ARTICLE

Multicenter interactions and ligand field effects in platinum(II) tripyrrindione radicals

Received 00th January 20xx,
Accepted 00th January 20xx

DOI: 10.1039/x0xx00000x

Elisa Tomat,*[a] Clayton J. Curtis,[a] Andrei V. Astashkin,[a] Jeanet Conradie,[b,c] and Abhik Ghosh*[c]

The tripyrrin-1,14-dione biopyrrin, which shares the scaffold of several naturally occurring heme metabolites, is a redox-active platform for metal coordination. We report the synthesis of square planar platinum(II) tripyrrindiones, in which the biopyrrin binds as a tridentate radical and the fourth coordination position is occupied by either aqua or *tert*-butyl isocyanide ligands. These complexes are stable through chromatographic purification and exposure to air. Electron paramagnetic resonance (EPR) data and density functional theory (DFT) analysis confirm that the spin density is located predominantly on the tripyrrindione ligand. Pancake bonding in solution between the Pt(II) tripyrrindione radicals leads to the formation of diamagnetic π dimers at low temperatures. The identity of the monodentate ligand (i.e., aqua vs isocyanide) affects both the thermodynamic parameters of dimerization and the tripyrrindione-based redox processes in these complexes. Isolation and structural characterization of the oxidized complexes revealed stacking of the diamagnetic tripyrrindiones in the solid state as well as a metallophilic Pt(II)–Pt(II) contact in the case of the aqua complex. Overall, the properties of Pt(II) tripyrrindiones, including redox potentials and intermolecular interactions in solution and in the solid state, are modulated through easily accessible changes in the redox state of the biopyrrin ligand or the nature of the monodentate ligand.

Introduction

Multicenter interactions between delocalized organic radicals involve the spin pairing between singly occupied molecular orbitals (SOMOs) to form diamagnetic π dimers.[1-3] These 'pancake bonds'[4] are investigated to provide insights into the fundamentals of multicentered bonding as well as to design compounds with novel electronic, magnetic, and optical properties for applications both in molecular systems and in materials science. For instance, pancake bonding interactions are being employed to develop organic conducting materials[5] and supramolecular assemblies.[6] Recent studies have primarily focused on purely organic radicals, such as cationic bipyridinium ($BIPY^{\bullet+}$) and tetrathiafulvalene ($TTF^{\bullet+}$) or neutral phenalenyl and verdazyl species (Chart 1).[1-2] The formation of dimers of metalloporphyrin radicals, however, has been recognized in early studies of this type of interactions in the 1970s.[7-9] The dimerization of zinc octaethylporphyrin radical cations ($[Zn(OEP^{\bullet})]^+$, Chart 1) was indeed described as the formation of a "new type of nonclassical bond".[9]

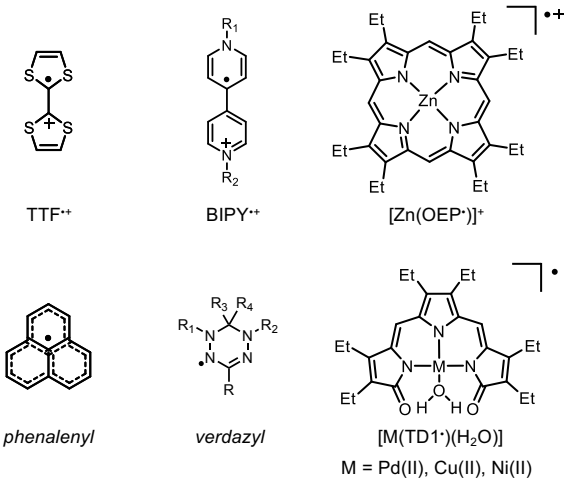

Chart 1. Examples of radical species that form multicenter bonding interactions.

Electron transfer involving metalloporphyrin radicals has been studied extensively with the goal, at least initially, of understanding and reproducing the redox photochemistry of natural photosynthetic systems.[10-13] More broadly, the interactions between porphyrin radicals remain at the center of an active area of investigation.[14-19]

The ability to host unpaired spins in stable open-shell systems at room temperature is also a characteristic of various macrocyclic oligopyrroles[20] as well as linear conjugated oligopyrroles, such as biliverdin and other bilindiones.[21] Several complexes of biopyrrin ligands, which present the structure of tripyrrolic and dipyrrolic heme metabolites, also exhibit a rich

[a] *Department of Chemistry and Biochemistry, The University of Arizona, 1306 E. University Blvd., Tucson, AZ 85721-0041, USA. Email: tomat@arizona.edu*
[b] *Department of Chemistry, University of the Free State, Bloemfontein 9300, Republic of South Africa.*
[c] *Department of Chemistry, UiT – The Arctic University of Norway, N-9037 Tromsø, Norway. Email: abhik.ghosh@uit.no*

† Footnotes relating to the title and/or authors should appear here.
Electronic Supplementary Information (ESI) available: Optical absorption and NMR data, crystallographic details, variable-temperature EPR data, cartesian coordinates from DFT calculations. See DOI: 10.1039/x0xx00000x

ligand-based redox chemistry on more compact π-systems that allow for the coordination of additional ligands.[22-24] The tripyrrin-1,14-dione ligand (H_3TD1) coordinates divalent transition metals as a dianionic radical ([M^{II}(TD1$^{\bullet}$)(H_2O)], Chart 1), and the open-shell π-system is stable when exposed to air at room temperature.[25-28] Reversible one-electron processes have allowed the isolation of complexes in three different redox states of the tridentate ligand,[25] and Zn(II) coordination produced a luminescent radical.[28-29] In variable-temperature experiments, we have shown that Cu(II)- and Pd(II)-bound tripyrrindione radicals reversibly form *π*-dimers resulting from multicentered interactions and antiferromagnetic coupling between the ligand-based unpaired spins.[27]

Here, we report the synthesis of Pt(II) tripyrrindione complexes featuring two different monodentate ligands (i.e., aqua and *tert*-butyl isocyanide) within the primary coordination sphere. The kinetic inertness of the Pt(II) center with respect to ligand exchange affords a robust platform to examine the influence of the monodentate ligand on the redox properties and π-dimerization of tripyrrindione radicals. In addition, we sought to assess a potential contribution from d^8–d^8 metallophilic interactions, which have been employed in the design of supramolecular assemblies and photofunctional materials based on Pt(II) complexes.[30-31] The multicentered interactions between Pt(II) tripyrrindione radicals were investigated experimentally in the solid state and in solution, as well as computationally by DFT methods. In addition, the one-electron oxidation products were included in this investigation as diamagnetic comparisons lacking the ligand-based radical.

Results and Discussion

Whereas the previously reported tripyrrindione complexes ([M(TD1$^{\bullet}$)(H_2O)], Chart 1) featured an all-ethyl β substitution (i.e., H_3TD1 ligand), here we opted to utilize the analogous 2,7,8,13-tetraethyl-3,12-dimethyl tripyrrin-1,14-dione (i.e., H_3TD2, Scheme 1) prepared from the commercially available 3-ethyl-4-methylpyrrolidin-2-one precursor (see ESI for experimental details).

Synthesis and characterization of neutral complexes

Although lighter group-10 cations Ni(II) and Pd(II) bind the tripyrrindione ligand readily at room temperature, the coordination of Pt(II) required more forcing conditions involving higher temperature and the presence of a base (Scheme 1). In addition, particularly in the case of isocyanide coordination, we performed the reaction under anhydrous conditions so as to maintain control of the fourth coordination position and avoid binding of an adventitious water molecule, which cannot be easily displaced from the [M(TD1$^{\bullet}$)(H_2O)] complexes. The coordination to platinum(II) was therefore accomplished by heating a solution of H_3TD2 in DMSO in the presence of K_2PtCl_4 (1.1 equiv) and K_2CO_3 (3 equiv) under an inert atmosphere. Upon heating for 90 minutes, the color of the solution changed from red to blue: the UV-visible absorption profile of this mixture indicated clear consumption of the free ligand concurrent with the growth of bands at 627 and 588 nm (Figure S1A). This intermediate complex, which was tentatively assigned as a platinum tripyrrindione with a coordinated DMSO, was not isolated as it readily converts to the aqua complex [Pt(TD2$^{\bullet}$)(H_2O)] (Scheme 1) in the presence of trace water. Conversely, in dry dichloromethane, treatment of the DMSO adduct with *tert*-butyl isocyanide leads to [Pt(TD2$^{\bullet}$)(*t*BuNC)] (Scheme 1), which is stable through aqueous workup and chromatography.

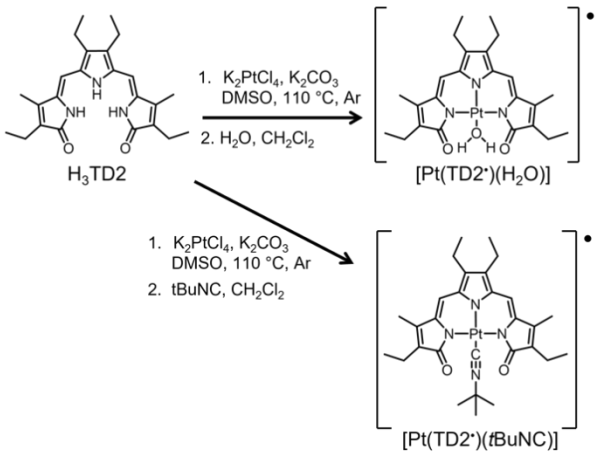

Scheme 1. Synthesis of Pt(II) tripyrrindione complexes.

The UV-visible absorption spectra of [Pt(TD2$^{\bullet}$)(H_2O)] and [Pt(TD2$^{\bullet}$)(*t*BuNC)] in dichloromethane display intense absorption bands at 592 and 602 nm, respectively (Figure S1B), as well as three weak near-IR transitions between 700 and 950 nm that are characteristic of tripyrrindione radicals.[25, 27]

An X-ray crystallographic analysis of [Pt(TD2$^{\bullet}$)(H_2O)] and [Pt(TD2$^{\bullet}$)(tBuNC)] (Figure 1, Tables S1, S2) revealed neutral complexes analogous to the previously examined complexes of hexaethyltripyrrin-1,14-dione.[25-28] The C–O bond lengths (1.243(4)–1.247(4) Å, aqua; 1.226(7)–1.235(6) Å, tBuNC; Table S2) are consistent with tripyrrindione bound as a dianionic radical.[25] The structure of [Pt(TD2$^{\bullet}$)(H_2O)] also displays intramolecular hydrogen-bonding interactions between these carbonyl groups and the aqua ligand, with internuclear donor–acceptor distances of 2.505 and 2.509 Å.

Complexes [Pt(TD2$^{\bullet}$)(H_2O)] and [Pt(TD2$^{\bullet}$)(tBuNC)] were modeled by DFT calculations using OLYP, B3LYP, and B3LYP* functionals, the D3 dispersion correction, and all-electron STO-TZ2P basis sets. A C_s symmetry constraint (with the mirror plane containing the Pt1-N2 bond and perpendicular to the mean plane of the TD2 ligand) was generally used. The key results were checked against symmetry-unconstrained calculations, and the differences were found to be insignificant. Consistent with EPR results (*vide infra)*, the calculated spin density profiles and SOMOs indicate essentially ligand-based radicals with only about 3-5% of the unpaired spin density on the metal (Figure 1). The optimized bond distances are in generally good agreement with the X-ray structures (Figure S2).

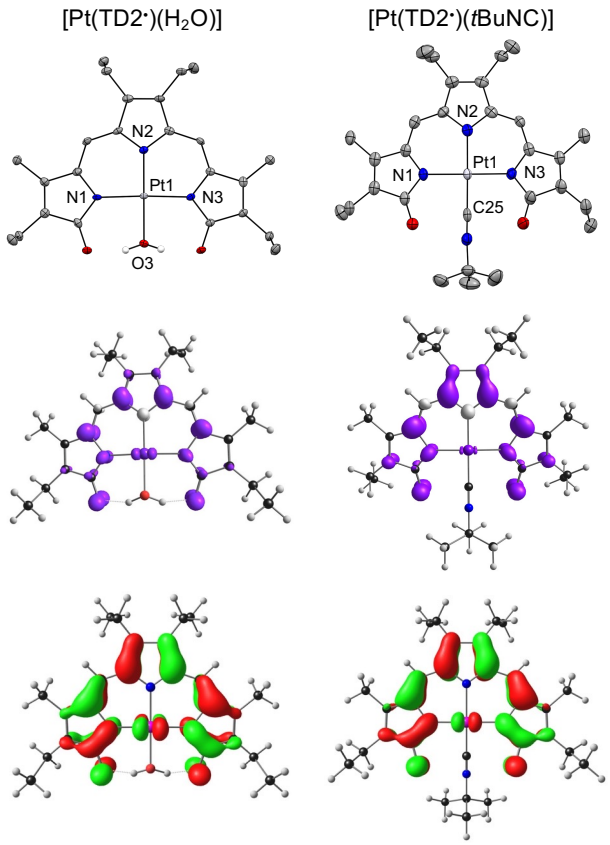

Figure 1. Crystallographic and computational analysis of [Pt(TD2•)(H_2O)] and [Pt(TD2•)(tBuNC)] (CCDC: 2182030) In the crystal structures (top panels), the carbon-bound hydrogen atoms are omitted for clarity, and non-hydrogen atoms are displayed as thermal displacement ellipsoids set at the 50% probability level (CCDC: 2182028 and 2182030). The spin density distributions (middle) show the α and β spin densities in purple and ivory, respectively.

Similar to other planar complexes of tripyrrindione radicals,[25-28] π-dimers are observed in the crystal lattice for both Pt(II) complexes, with antiparallel orientation and mean interplanar separations of ~3.3 Å (Figure 2). Significant lateral shifts lead to Pt–Pt distances of 4.614 Å and 4.884 Å for [Pt(TD2•)(H_2O)] and [Pt(TD2•)(tBuNC)], respectively. As in the case of Pt(II) bis(phenolate)dipyrrinato radicals,[32] these π-dimers do not involve Pt–Pt metallophilic interactions in the solid state. In spite of the structural similarity of the [Pt(TD2•)(H_2O)] and [Pt(TD2•)(tBuNC)] π-dimers, the larger isocyanide ligand may hinder the interaction between the π-systems: the significantly increased lateral shift is likely indicative of decreased overlap in the solid state. The dimerization between these tripyrrindione radicals in solution was investigated by EPR methods.

The room-temperature EPR spectrum of [Pt(TD2•)(H_2O)] in toluene presents a single isotropic line at $g \approx 2.004$ (blue trace, Figure 3a). In contrast, the room-temperature spectrum of [Pt(TD2•)(tBuNC)] is centered at $g \approx 2.006$ and shows a resolved triplet (purple trace, Figure 3a) caused by the isotropic hyperfine interaction (*hfi*) with the ^{195}Pt nucleus (I = ½, natural abundance 33.8%). Although both EPR spectra are indicative of a predominantly ligand-based unpaired electron, a minor spin delocalization on the metal is evident from the shifts of the isotropic g-factor from the free electron g-value of 2.0023 and from the non-zero ^{195}Pt *hfi*. These data are in qualitative agreement with the DFT calculation results (Figures 1 and S2).

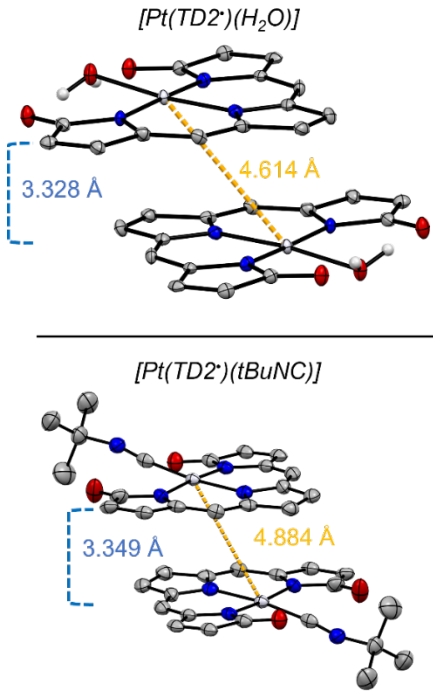

Figure 2. Dimeric structural units in the crystal packing of Pt(II)-tripyrrindione radicals (top, aqua; bottom tBuNC). Ethyl and methyl substituents and carbon-bound hydrogen atoms are omitted for clarity. Non-hydrogen atoms are displayed as thermal displacement ellipsoids set at the 50% probability level (CCDC: [(Pt(TD2•)(H_2O)], 2182028; [(Pt(TD2•)(tBuNC)], 2182030).

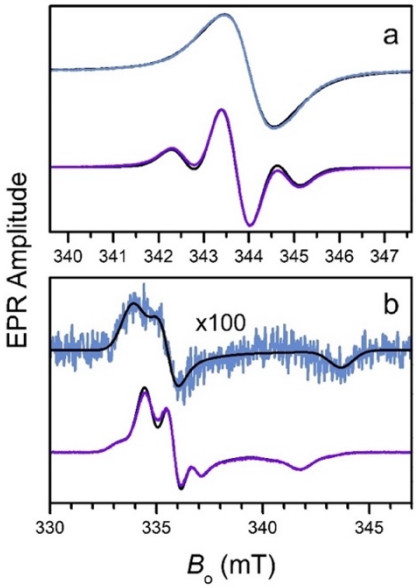

Figure 3. Experimental EPR spectra of [Pt(TD2•)(H_2O)] (blue) and [Pt(TD2•)(tBuNC)] (purple) in liquid toluene solution at room temperature (a) and frozen glassy toluene solution at 77 K (b). Experimental conditions at room temperature: mw frequency, 9.650 GHz; mw power, 0.2 mW; modulation amplitude, 0.1 mT. Experimental conditions at 77 K: mw frequency, 9.465 GHz; mw power, 0.2 mW; modulation amplitude, 0.1 mT. Black traces show the simulated spectra (simulation parameters are listed in Table S3).

The pronounced *g*-anisotropy of the spectra in frozen solutions (Figure 3b, Table S3) is also consistent with spin

delocalization on the Pt(II) center and similar to that reported for platinum complexes with a ligand-based unpaired electron[33-35] (but much smaller than that observed in Pt(I) and Pt(III) complexes).[36] Notably, the signal of [Pt(TD2•)(H_2O)] in frozen toluene at 77 K (Figure 3b, blue trace) is almost completely quenched, whereas the low-temperature signal of [Pt(TD2•)(tBuNC)] is reduced to a much lesser extent and shows semiresolved ^{195}Pt *hfi* features (Figure 3b, purple trace). These observations are examined in the next section in the context of the expected formation of antiferromagnetically coupled π-dimers.

Given the expected near-identical spin density distributions across the tripyrrindione ligand in [Pt(TD2•)(H_2O)] and [Pt(TD2•)(tBuNC)] complexes (Figure 1), the significant difference in the appearance and width of the room-temperature EPR spectra warranted further analysis. Based on our calculations to obtain simulated spectra (Figure 3, black lines, see ESI for details), we attribute this difference to a combination of several factors: (i) a decrease in the ^{195}Pt *hfi* constant, (ii) a dynamic exchange interaction between the [Pt(TD2•)(H_2O)] complexes in solution, and (iii) a decrease in the transverse relaxation time, T_2. The detectable effect of dynamic spin exchange for the [Pt(TD2•)(H_2O)] complex correlates with the greater propensity of this complex (compared to [Pt(TD2•)(tBuNC)]) to forming π-stacked dimers at low temperatures (see below). This effect is positively correlated with the lifetime of the transient dimers in liquid solution, which is determined by the thermodynamic parameters of dimerization.

Dimerization of neutral tripyrrindione radicals in solution

The multicenter bonding and formation of Pt(II) tripyrrindione π-dimers was investigated *via* variable-temperature EPR measurements. The EPR spectra of [Pt(TD2•)(H_2O)] and [Pt(TD2•)(tBuNC)] in toluene (0.8 and 1.0 mM, respectively) were recorded at nonsaturating microwave (mw) power levels between 340 K and 140 K (Figure S3). The double integrals of these spectra over the magnetic field were multiplied by the absolute temperature to obtain the relative spin concentrations as a function of temperature (Figure 4, top panel). Within the temperature range examined, a near-complete quenching of the EPR signal was observed for [Pt(TD2•)(H_2O)] in toluene; however, we observed only ~20% reduction in temperature-corrected signal intensity for [Pt(TD2•)(tBuNC)] at the lowest measured temperatures (Figure S3). To increase the measurable temperature window and potentially observe further dimerization of [Pt(TD2•)(tBuNC)], we performed the experiments in a 1:3 (*v/v*) mixture of toluene and methylcyclohexane (MCH), which has a lower melting point compared to neat toluene. Unexpectedly, this change in solvent environment resulted in ~80% quenching of the EPR signal for [Pt(TD2•)(tBuNC)] over the measured temperature range. In contrast, for [Pt(TD2•)(H_2O)] the change in solvent conditions had little impact on dimer formation.

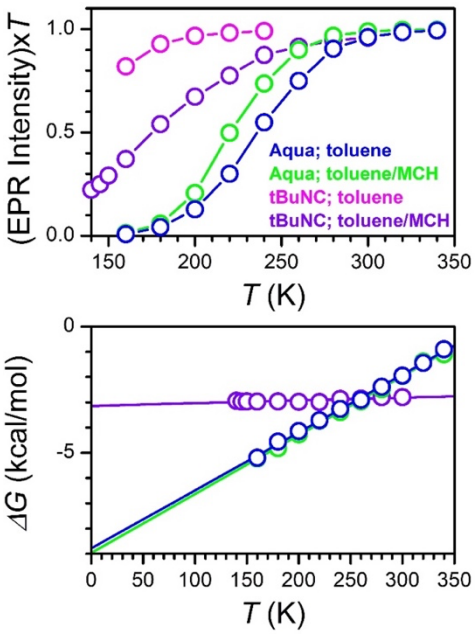

Figure 4. Temperature dependences of relative EPR intensity (top panel) and Gibbs free energy of dimerization (bottom panel) of [Pt(TD2•)(H_2O)] (blue, green) and [Pt(TD2•)(tBuNC)] (magenta, purple). The data were obtained by EPR measurements in toluene or in a 1:3 (v/v) mixture of toluene and methylcyclohexane (MCH). The complex concentrations were: 0.8 mM [Pt(TD2•)(H_2O)] in toluene, 0.2 mM [Pt(TD2•)(H_2O)] in toluene/MCH, 1 mM [Pt(TD2•)(tBuNC)] in toluene, and 0.2 mM [Pt(TD2•)(tBuNC)] in toluene/MCH. The free energy temperature dependence for [Pt(TD2•)(tBuNC)] in toluene is not presented because the change of EPR intensities in the accessible temperature range was too small to allow for an accurate derivation.

Table 1. Thermodynamic parameters of dimerization obtained from the EPR data (Figure 4)

Complex & solvent	ΔH (kcal·mol^{-1})	ΔS (cal·mol^{-1}·K^{-1})
[Pt(TD2•)(H_2O)] in toluene	-8.8 ± 0.4	-23 ± 1
[Pt(TD2•)(H_2O)] in toluene/MCH	-9.0 ± 0.4	-23 ± 1
[Pt(TD2•)(*t*BuNC)] in toluene/MCH	-3.1 ± 0.2	-1.1 ± 0.4

The temperature-dependent spin concentrations (i.e., the concentrations of the radical monomers) were used to estimate the equilibrium constants for dimer formation and the Gibbs free energy of dimerization (Figure 4, bottom panel and Table 1). The thermodynamic parameters for dimerization of [Pt(TD2•)(H_2O)] displayed no solvent dependence, and the ΔH and ΔS values were similar to those of Pd(II) and Cu(II) tripyrrindiones.[27] These findings were also within the range generally observed for octaethylporphyrin radical cations[37] and other charged and neutral organic radicals.[38] The rather large and negative entropic contribution is expected for dimerization reactions and accounts for the equilibrium shift towards the dimer as the temperature decreases.

For the isocyanide complex, the small number of data points in toluene did not allow for reliable calculations. In the toluene/methylcyclohexane mixture, the enthalpy of dimerization for [Pt(TD2•)(tBuNC)] is smaller by ~6 kcal mol^{-1} relative to that of the aqua complex, and the entropic change is almost negligible. The weaker thermodynamic drive to dimerization can be attributed qualitatively to a less effective overlap between the isocyanide complexes as observed in the single-crystal structure (Figure 2). In addition, the solvent dependence and minimal entropic change point to a significant contribution from solvent reorganization effects associated to the larger isocyanide ligand. Indeed solvent effects on radical dimerization were found to be pronounced in the case of porphyrin[8] and dicyanodichlorobenzoquinone[38] radicals.

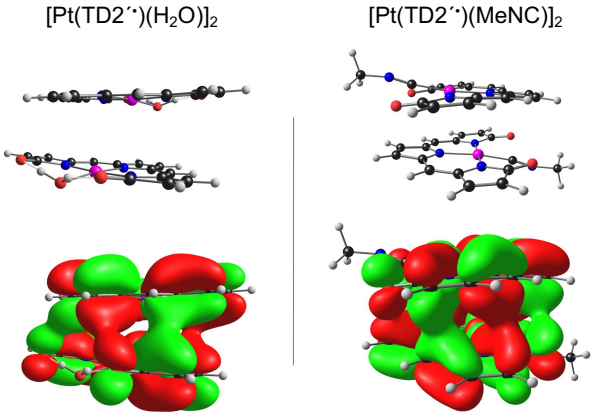

Figure 5. B3LYP-D3 optimized geometries and HOMOs of antiferromagnetically coupled neutral radical dimers. The simplified complexes [Pt(TD2´•)(H_2O)] and [Pt(TD2´•)(MeNC)] lack all the ethyl and methyl substituents and feature MeNC in place of *t*BuNC. The HOMOs depict the topology of the pancake bonding.

Broken-symmetry B3LYP-D3 DFT geometry optimizations on simplified model compounds (i.e., dimers of [Pt(TD2´•)(H_2O)] and [Pt(TD2´•)(MeNC)] lacking all the ethyl and methyl substituents and featuring MeNC in place of *t*BuNC) preferred antiferromagnetically coupled M_S = 0 solutions by 2-3 kcal/mol relative to the corresponding ferromagnetically coupled M_S = 1 solutions. The broken-symmetry spin density profiles clearly indicated that the radical character of the monomers also persists in the dimers and that the bonding between the monomers is best described as multicenter pancake bonding as observed for dimeric metalloporphyrin π-cation-radicals.[8-9, 37, 39] Rerunning the broken-symmetry geometries via a spin-restricted formalism and visualizing the HOMO provided a crude but effective means of visualizing the pancake interaction (Figure 5). No net metallophilic interaction between platinum centers was detected in these calculated structures.

Synthesis and characterization of cationic tripyrrindione complexes

The electrochemical profiles of [Pt(TD2•)(H_2O)] and [Pt(TD2•)(tBuNC)] in CH_2Cl_2 were investigated by cyclic voltammetry (Figure 6). [Pt(TD2•)(H_2O)] displayed two quasi-reversible events at –0.107 V and –0.701 V ascribed to one-electron oxidation and reduction of the tripyrrolic scaffold, respectively. The electrochemical profile of [Pt(TD2•)(tBuNC)] displayed a similar voltammogram; however, the reversible oxidation and reduction events were cathodically shifted to –0.338 V and –0.866 V, respectively. The half-wave redox potentials for the aqua Pt(II) complex are similar (within ~50 mV) to those of analogous Pd(II)[13] and Cu(II)[16] aqua complexes (Table S4), indicating that the electrochemical profile of the tripyrrindione framework is largely unperturbed when changing the central metal. Conversely, the significant cathodic shift of both oxidative and reductive events (~230 and ~160 mV, respectively) observed upon replacement of the aqua ligand with *t*-butyl isocyanide indicates that the redox activity of tripyrrindione can be tuned through modifications within the primary coordination sphere. In this comparison, the intramolecular hydrogen bonds between the aqua ligand and the carbonyl groups on the tripyrrindione are likely stabilizing the anionic complex. Consistent with this notion, our crystallographic and computational analysis of Pd(II)-aqua tripyrrindiones indicated that the hydrogen bonds are strongest in the anionic complex.[13]

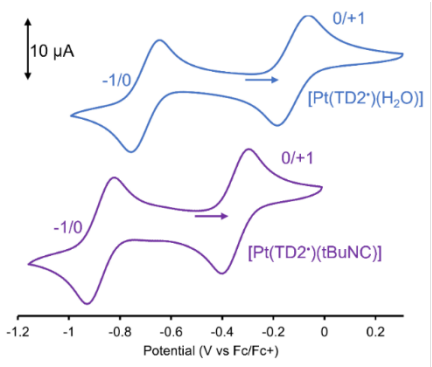

Figure 6. Cyclic voltammograms of [Pt(TD2•)(H_2O)] (blue) and [Pt(TD2•)(tBuNC)] (purple) in CH_2Cl_2 at 100mV/s. Potentials referenced to the ferrocene/ferrocenium (Fc/Fc^+) redox couple.

B3LYP-D3 DFT calculations yielded a significantly higher adiabatic ionization potential (IP) for [Pt(TD2•)(H_2O)] (5.92 eV) relative to [Pt(TD2•)(tBuNC)] (5.57 eV) as well as a slightly higher adiabatic electron affinity (EA), 2.26 vs. 2.17 eV, respectively. These calculated gas-phase IPs and EAs are in qualitative accord with electrochemical oxidation and reduction potentials, respectively, and underscore the impact of the monodentate ligand.

To examine the effect of the isocyanide ligand on the structures of the oxidized complexes, we sought to isolate the cationic products of ligand oxidation. Treatment of dichloromethane solutions of either [Pt(TD2•)(H_2O)] or [Pt(TD2•)(tBuNC)] with silver tetrafluoroborate resulted in the formation of the expected diamagnetic products, which were first characterized by NMR spectroscopy (Figures S4-S7). The ^{1}H and ^{13}C NMR spectra of the oxidized aqua complex, [Pt($TD2_{ox}$)(H_2O)][BF_4], displayed the anticipated resonances pertaining to a coordinated tripyrrindione (i.e., methine bridge singlets at 6.92 ppm (^{1}H) and 101.9 ppm (^{13}C)), and the bound aqua ligand was observed as a singlet at 9.81 ppm. Similarly, the

^{1}H NMR spectrum of the oxidized *tert*-butyl isocyanide complex, [Pt(TD2$_{ox}$)(tBuNC)][BF$_4$], presented a 2H resonance at 6.95 ppm for the methine bridges, a 9H singlet at 1.69 ppm corresponding to the bound *t*BuNC ligand.

Monitoring the oxidation reaction by UV-visible absorption spectroscopy revealed a shift of the main band of [Pt(TD2$^{\bullet}$)(H$_2$O)] from 592 nm to 549 nm and disappearance of the weak near-IR absorptions concurrent with the growth of a new broad peak at 682 nm (Figure S8, red trace). Chemical oxidation of [Pt(TD2$^{\bullet}$)(tBuNC)] also resulted in the disappearance of the near-IR bands between 700 and 950 nm, accompanied by broadening of the main band at ~600 nm (Figure S8, black trace).

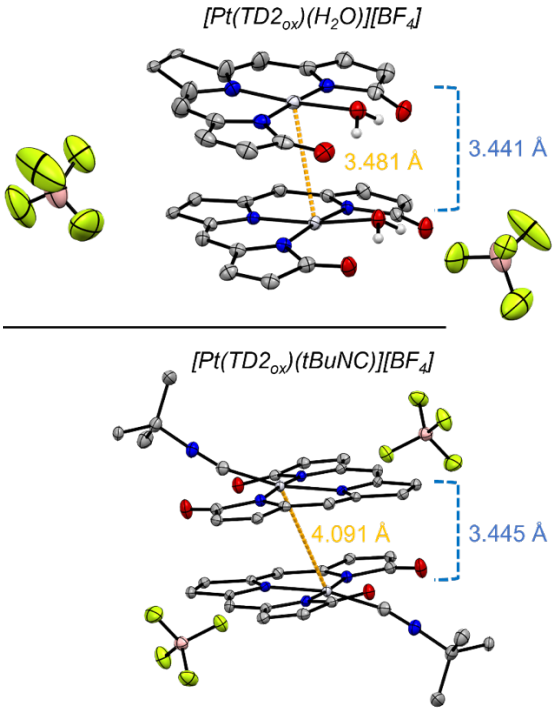

Figure 7. Dimeric structural units in the crystal packing of oxidized Pt(II)-tripyrrindione complexes (top, aqua; bottom tBuNC). Pt–Pt distances are shown in orange, and mean interplanar separations are shown in blue. Ethyl and methyl substituents and carbon-bound hydrogen atoms are omitted for clarity. Non-hydrogen atoms are displayed as thermal displacement ellipsoids set at the 50% probability level (CCDC: [Pt(TD2$_{ox}$)(H$_2$O)][BF$_4$], 2182029; [Pt(TD2$_{ox}$)(tBuNC)][BF$_4$], 2182027).

The structures of [Pt(TD2$_{ox}$)(H$_2$O)][BF$_4$] and [Pt(TD2$_{ox}$)(tBuNC)][BF$_4$] were analyzed by X-ray crystallography (Figure 7). For both complexes, the bond lengths within the tripyrrindione scaffold are consistent with one-electron oxidation of the ligand π-system (i.e., elongations and contractions of several C–N and C–O distances relative to the dianionic radical tripyrrindione, Table S2). In [Pt(TD2$_{ox}$)(H$_2$O)][BF$_4$], the hydrogen bonds between the aqua ligand and the carbonyl groups present longer donor-acceptor distances (i.e., 2.534–2.575 Å) relative to those in the neutral complex, thus indicating slightly weaker interactions. A comparison of the [Pt(TD2$_{ox}$)(*t*BuNC)]$^+$ structure to that of the parent radical complex (Figure S9) highlights a larger deviation from linearity of the Pt-C-N angle (from 173° to 166°) and a contraction of the C≡N isocyanide bond (from 1.170(6) to 1.155(4) Å). These structural changes in the case of the cationic complex are consistent with more pronounced σ donation from the carbon lone pair, which is primarily antibonding with respect to the C≡N isocyanide bond.[40]

The asymmetric unit in the [Pt(TD2$_{ox}$)(H$_2$O)][BF$_4$] crystal contains two complexes in parallel orientation, with the two tripyrrindione ligand planes nearly eclipsed, in contrast to all previously studied tripyrrindione complexes that were found to form antiparallel dimers. This alteration in packing morphology is not supported by intermonomer hydrogen bonds and is concurrent with a short Pt–Pt contact (i.e., 3.481 Å) indicative of a metallophilic interaction arising from the overlap of predominatly d_{z2} orbitals, which is typically associated with Pt–Pt distances below ~3.5 Å.[41-43] In contrast, the crystal packing of [Pt(TD2$_{ox}$)(*t*BuNC)][BF$_4$] maintains the more common antiparallel orientation and shows a shortening of the Pt–Pt distance from 4.884 Å (neutral radical) to 4.091 Å (oxidized cation) but not reaching the contact of a typical Pt(II)–Pt(II) interaction (Figure 7).

When compared to the neutral Pt(II)-tripyrrindione radicals, the cationic dimers in the solid state (Figure 7) show only a slight increase of the interplanar distance (from ~3.3 to ~3.4 Å) in spite of the electrostatic repulsion. Indeed, metallophilic Pt(II)–Pt(II) interactions and π-stacking effects are characteristic of the crystal packing of planar Pt(II) complexes with large aromatic ligands,[41-43] and their interplay likely leads to different orientations and/or overlaps of the tripyrrindione frameworks for these cationic dimers of closed-shell oxidized complexes.

We conducted B3LYP-D3 calculations on the simplified oxidized dimers [Pt(TD2´$_{ox}$)(H$_2$O)]$_2^{2+}$ (C_s, with the plane of symmetry perpendicular to the mean tripyrrindione planes) and [Pt(TD2´$_{ox}$)(MeNC)]$_2^{2+}$ (C_i) starting approximately from the crystallographic orientation and allowing optimization to the nearest local minima. The resulting structures (which do not include BF$_4^-$ counterions) revealed a major influence of oxidation on both the geometry of the monomeric units and on the separation between the monomers. Oxidation relieved several antibonding interactions in the TD2´ (or TD2) radicals, especially along the C$_\alpha$-N-C$_\alpha$-O stretches of the outer pyrrolinone rings, thereby accentuating bond length alternation in these parts of the molecule relative to the neutral monomeric complexes. In addition, a shrinkage in calculated Pt–Pt separations is observed in agreement with the crystal structures (Figure 7). It is worth noting, however, that DFT calculations, as a single-determinant method, cannot definitively confirm the existence and importance of a possible metallophilic interaction; such confirmation can only come from high-level ab initio correlated calculations.[44]

A careful examination of the occupied valence MOs of the two dicationic dimers qualitatively identified them as derived entirely from pairwise bonding and antibonding interactions of the monomers' occupied MOs (Figures S10-S11). No occupied MO provided an obvious rationale for the significant intermonomer bonding observed for the oxidized dimers in the solid state, which thus emerges as a multideterminantal effect. The excellent quality of the optimized geometries suggests that DFT does capture the effect in a 'rough and ready' manner, but

an identification of the specific Slater determinants involved must await a full multireference study. We considered the possibility that the intermonomer bonding in the oxidized dimers might lie in so-called double pancake bonding,[45] which has been invoked for antiaromatic or diradicaloid compounds such as norcorrole.[46-47] However, B3LYP-D3 calculations on both oxidized monomers and dimers revealed substantial singlet-triplet gaps > 0.7 eV, so these species do not really qualify as diradicaloids.

Experimental

Materials and Methods

Dichloromethane (CH_2Cl_2), acetonitrile (CH_3CN), and pentane were dried by passage through a solvent purifier. Dimethyl sulfoxide (DMSO) was thoroughly dried over activated 4 Å molecular sieves. All other commercial reagents were used without further purification. NMR spectra were recorded on a Bruker NEO-500 MHz NMR spectrometer at the NMR Spectroscopy Facility of the Department of Chemistry and Biochemistry at The University of Arizona. UV–visible spectra were obtained at ambient temperature using an Agilent 8453 UV–vis spectrophotometer. High-resolution mass spectra (HRMS) *via* electrospray ionization (ESI) methods were obtained at the University of Arizona Analytical and Biological Mass Spectrometry Core Facility. Elemental analyses were performed by NuMega Resonance Laboratories in San Diego, CA.

Synthetic Procedures

H_3TD2 (2,7,8,13-Tetraethyl-3,12-dimethyl-15H,17H-tripyrrin-1,14-dione). 3,4-Diethyl-2,5-diformyl-1*H*-pyrrole (0.380 g, 2.120 mmol) and 3-ethyl-4-methyl-3-pyrrolin-2-one (0.795 g, 6.351 mmol) were dissolved in CH_3CN (15 mL) in a pressure vessel with 1,8-diazabicyclo(5.4.0)undec-7-ene (DBU) (3.6 mL, 24.07 mmol). The vessel was capped and heated in an oil bath at 120 °C for 24 h. After cooling to room temperature, the reaction mixture was diluted with CH_2Cl_2 (60 mL) and washed with 20% aq. HCl (120 mL) in a separatory funnel. The organic layer was subsequently washed with brine (3 x 50 mL), dried over Na_2SO_4, and the solvent was removed under reduced pressure. The crude solid was purified *via* flash chromatography (10/90 to 100/0, v/v, hexanes/ethyl acetate) to afford H_3TD2 as a red solid (0.509 g, 61 %). UV-vis (CH_2Cl_2) λ_{max} (ε): 322 (34,700), 487 (21,400 M^{-1} cm^{-1}). ^{1}H NMR (500 MHz, $CDCl_3$): δ 10.47 (s, 1H), 9.62 (s, 1H), 6.02 (s, 1H), 2.55 (q, *J* = 7.6 Hz, 4H), 2.18 (q, *J* = 7.6 Hz, 4H), 2.04 (s, 6H), 1.18 (t, *J* = 7.5 Hz, 6H), 0.92 (t, *J* = 7.5 Hz, 6H). ^{13}C NMR (125 MHz, $CDCl_3$): δ 174.41, 141.18, 134.14, 131.80, 130.11, 128.82, 99.13, 17.83, 16.92, 16.68, 13.47, 9.81. HRMS-ESI$^+$ (*m/z*): $[M+H]^+$: calcd. for $[C_{24}H_{32}N_3O_2]^+$: 394.2489; found: 394.2485.

[Pt(TD2$^\bullet$)(H_2O)]. H_3TD2 (29 mg, 0.073 mmol), K_2PtCl_4 (33 mg, 0.081 mmol), and K_2CO_3 (30 mg, 0.218 mmol) were dissolved in dry DMSO (0.4 mL) and heated at 110 °C for 2 h under an argon atmosphere. Upon consumption of free H_3TD2, as determined through UV–visible absorption spectroscopy, the reaction was cooled to room temperature. The navy blue reaction mixture was diluted with CH_2Cl_2 (3 mL) and stirred open to air for 1 hour to allow for complete oxidation to the radical product. The reaction mixture was diluted with CH_2Cl_2 (20 mL), washed in a separatory funnel with brine (3 x 30 mL), dried over Na_2SO_4, and the solvent was removed *in vacuo*. The crude solid was purified *via* flash chromatography (0/100 to 35/65, v/v, hexanes/ethyl acetate) to afford [Pt(TD2$^\bullet$)(H_2O)] as a royal blue solid (25 mg, 57%). UV-vis (CH_2Cl_2) λ_{max} (ε): 305 (32,400), 405 (9,800), 453 (8,400), 508 (6,800), 553 (13,000), 592 (42,200), 672 (4,500), 769 (2,800), 960 (2,600 M^{-1} cm^{-1}). HRMS-ESI$^+$ (*m/z*): $[M]^+$ calcd. for $[C_{24}H_{30}N_3O_3Pt]$: 603.1935; found: 603.1942. Anal. Calcd. for $[C_{24}H_{30}N_3O_3Pt]$: C, 47.8; N, 5.0; H, 6.9 %; found, C, 48.0; N, 4.8; H, 6.7 %.

[Pt(TD2$^\bullet$)(tBuNC)]. H_3TD2 (55 mg, 0.141 mmol), K_2PtCl_4 (65 mg, 0.157 mmol), and K_2CO_3 (58 mg, 0.420 mmol) were dissolved in dry DMSO (0.5 mL) and heated at 110 °C for 2 h under an argon atmosphere. Upon consumption of free H_3TD2, as determined through UV–visible absorption spectroscopy, the reaction was cooled to room temperature. tBuNC (16 µL, 0.141 mmol) was dissolved in CH_2Cl_2 (3 mL) and added to the reaction mixture, which was stirred at room temperature under argon for 1 h. The navy blue solution was opened to air and stirred for an additional 2 h to allow for complete oxidation to the radical product. The reaction mixture was diluted with CH_2Cl_2 (30 mL), washed in a separatory funnel with brine (3 x 30 mL) and dried over Na_2SO_4, then the solvent was removed *in vacuo*. The crude solid was purified *via* flash chromatography (0/100 to 35/65, v/v, hexanes/ethyl acetate) to afford [Pt(TD2$^\bullet$)(tBuNC)] as a sapphire blue solid (57 mg, 61%). UV-vis (CH_2Cl_2) λ_{max} (ε): 398 (15,000), 512 (7,300), 603 (33,000), 768 (2,300), 826 (2,900), 940 (6,900 M^{-1} cm^{-1}). HRMS-ESI$^+$ (*m/z*): $[M]^+$ calcd. for $[C_{29}H_{37}N_4O_2Pt]$, 668.2564; found, 668.2563. Anal. Calcd. for $[C_{29}H_{37}N_4O_2Pt]$: C, 52.1; N, 5.6; H, 8.4 %; found, C, 51.5; N, 5.3; H, 8.0 %.

[Pt(TD2$_{ox}$)(H_2O)][BF_4]. [Pt(TD2$^\bullet$)(H_2O)] (10.6 mg, 0.018 mmol) was dissolved in CH_2Cl_2 (4 mL), and solid $AgBF_4$ (6.5 mg, 0.033 mmol) was added at room temperature. The reaction was stirred for 10 minutes until full conversion was determined *via* UV–visible absorption spectroscopy and filtered through a medium frit funnel to remove elemental silver. The solvent was then removed *in vacuo*, and the crude solid was purified by crystallization from a layered solution of CH_2Cl_2/pentane to afford [Pt(TD2$_{ox}$)(H_2O)][BF_4] as a red solid (8.3 mg, 68%). UV-vis (CH_2Cl_2) λ_{max} (ε): 303 (24,800), 421 (5,700), 549 (23,500), 682 (4,400 M^{-1} cm^{-1}). ^{1}H NMR (500 MHz, $CDCl_3$): δ 9.81(s, 2H), 6.92 (s, 2H), 2.81 (q, *J* = 7.6 Hz, 4H), 2.49 (s, 3H), 2.31 (q, *J* = 7.6 Hz, 4H), 1.26 (t, *J* = 7.6 Hz, 6H), 1.18 (t, *J* = 7.6 Hz, 6H); ^{13}C NMR (125 MHz, $CDCl_3$): δ 188.5, 163.3, 157.6, 150.2, 148.5, 139.3, 101.9, 18.4, 17.8, 15.6, 12.4, 10.3. Anal. Calcd. for $[C_{24}H_{30}BF_4N_3O_3Pt]$: C, 41.8; N, 4.4; H, 6.1 %; found, C, 41.4; N, 4.0; H, 5.8 %.

[Pt(TD2$_{ox}$)(tBuNC)][BF_4]. [Pt(TD2$^\bullet$)(tBuNC)] (13.2 mg, 0.020 mmol) was dissolved in CH_2Cl_2 (4 mL), and solid $AgBF_4$ (7.2 mg, 0.037 mmol) was added at room temperature. The reaction was stirred for 10 minutes until full conversion was determined *via* UV–visible absorption spectroscopy and then filtered through a medium frit funnel to remove Ag. The solvent was removed *in vacuo*, and the crude solid was purified by crystallization from a layered solution of CH_2Cl_2/pentane to afford [Pt(TD2$_{ox}$)(tBuNC)][BF_4] as a blue solid (10.4 mg, 70%). UV-vis

(CH_2Cl_2) λ_{max} (ε): 294 (20,900), 331 (14,300), 384 (6,200), 516 (12,900), 602 (12,700 M^{-1} cm^{-1}). ^1H NMR (500 MHz, $CDCl_3$): δ 6.95 (s, 2H), 2.88 (q, *J* = 7.7 Hz, 4H), 2.45 (s, 6H), 2.42 (q, *J* = 7.7 Hz, 4H), 1.69 (s, 9H), 1.31 (t, *J* = 7.7 Hz, 6H), 1.19 (t, *J* = 7.7 Hz, 6H); ^{13}C NMR (125 MHz, $CDCl_3$): δ 179.5, 163.7, 158.7, 148.5, 147.8, 137.1, 99.9, 58.5, 29.8, 18.3, 18.2, 15.6, 12.8, 10.5. Anal. Calcd. for [$C_{29}H_{37}BF_4N_4O_2Pt$]: C, 46.1; N, 4.9; H, 7.4 %; found, C, 45.8; N, 4.7; H, 7.1 %.

X-ray Diffraction Analysis

The single-crystal X-ray diffraction measurements were performed at the XRD facility of the University of Arizona, Department of Chemistry and Biochemistry, on a Bruker Kappa APEX II Duo diffractometer equipped with APEX II CCD area detector, four-circle kappa goniometer, and an Oxford Cryostream low-temperature system. The data collection was performed at 100 K, using the Mo K_α radiation (λ = 0.71073 Å). During the measurements, the instrument was controlled by the APEX2 software package (Bruker AXS Inc., Madison, WI, 2007). The absorption correction was done using a multiscan method implemented in SADABS (Sheldrick, G. M.; University of Göttingen, Germany, 1997).

The crystal structures were solved and refined using the *SHELX* package called from the *Olex2* GUI. All non-H atoms were located in the Fourier map and were refined anisotropically. The carbon-bound hydrogen atoms were calculated in ideal positions with isotropic displacement parameters set to 1.2U_{eq} of the host atom (1.5U_{eq} for methyl hydrogen atoms); their positions were then refined using a riding model.

Structure refinement of [Pt(TD2•)(H_2O)]. Crystals grew as red plates by slow diffusion of pentane into CH_2Cl_2 at room temperature. The structure was solved and refined in the monoclinic space group $P2_1/n$. The asymmetric unit cell contained one complete complex molecule. Q-peaks for hydrogen-bonded OH protons were located in the Fourier map: hydrogen atoms were assigned to those positions and refined explicitly. The highest residual Fourier peak found in the model was +1.21 *e* Å^{-3} approximately 0.87 Å from Pt1, and the deepest Fourier hole was –0.91 *e* Å^{-3} approximately 0.86 Å from Pt1.

Structure refinement of [Pt(TD2•)(tBuNC)]. Crystals grew as red plates by slow diffusion of pentane into CH_2Cl_2 at room temperature. The structure was solved and refined in the monoclinic space group $P2_1/n$. The asymmetric unit cell contained one complete complex molecule. In order to satisfy a B-level CheckCIF alert for a Q-peak at a chemically unreasonable position, the Pt1 atom was modelled with 5% occupancy over two positions. The highest residual Fourier peak found in the model was +0.77 *e* Å^{-3} approximately 1.02 Å from H15B, and the deepest Fourier hole was –0.44 *e* Å^{-3} approximately 1.38 Å from H23A.

Structure refinement of [Pt($TD2_{ox}$)(H_2O)][BF_4]. Crystals grew as red plates by slow diffusion of pentane into CH_2Cl_2 at room temperature. The structure was solved and refined in the triclinic space group P-1. The asymmetric unit cell contained two crystallographically distinct complex molecules. Q-peaks for hydrogen-bonded OH protons were located in the Fourier map, and hydrogens were assigned to those positions and refined explicitly. Six carbon atoms of one tripyrrindione ligand (C7B, C8B, C18B, C19B, C20B, and C21B) were found to be disordered and were modeled by a distribution over two positions. The highest residual Fourier peak found in the model was +1.57 *e* Å^{-3} approximately 0.84 Å from Pt1B, and the deepest Fourier hole was –1.06 *e* Å^{-3} approximately 0.71 Å from Pt1A.

Structure refinement of [Pt($TD2_{ox}$)(tBuNC)][BF_4]. Crystals grew as blue plates by slow diffusion of pentane into CH_2Cl_2 at room temperature. The structure was solved and refined in the monoclinic space group $P2_1/n$. The asymmetric unit cell contained one complete complex molecule. The highest residual Fourier peak found in the model was +1.31 *e* Å^{-3} approximately 0.76 Å from Pt1, and the deepest Fourier hole was –0.59 *e* Å^{-3} approximately 0.65 Å from Pt1.

EPR Analysis

The EPR experiments were carried out at the University of Arizona EPR Facility on an X-band EPR spectrometer Elexsys E500 (Bruker). The measurements at liquid nitrogen temperature were conducted using a finger dewar. The variable temperature measurements were performed using the cryogenic nitrogen gas flow system ER 4111VT (Bruker). The analysis of the variable temperature EPR data to obtain the thermodynamic parameters pertaining to the dimerization of the complexes was conducted as previously reported.[27]

Electrochemical Analysis

Cyclic voltammograms were performed on a Gamry Reference 600 potentiostat utilizing a single-compartment cell with three electrodes: a glassy carbon working electrode, a platinum wire auxiliary electrode, and a $Ag/AgNO_3$ quasi-reference electrode. Measurements were performed at ambient temperature under an inert argon atmosphere in CH_2Cl_2 containing 0.1 M (NBu_4)(PF_6) (triply recrystallized) as a supporting electrolyte. Sample concentrations were 1–2 mM, and all electrochemical data were internally referenced to the ferrocene/ferrocenium couple (set at 0.00 V).

Computational Methods

Scalar-relativistic DFT calculations with the ZORA Hamiltonian[48-49] and all-electron STO-TZ2P ZORA basis sets were carried out with the OLYP[50-51] and B3LYP[52-53] (20% exchange), each augmented with D3 dispersion corrections,[54] all as implemented in ADF program system.[55] Carefully tested, fine integration grids and tight SCF and geometry optimization criteria were used throughout.

Conclusions

We developed synthetic methods to coordinate Pt(II) within the planar tridentate framework of tripyrrindione and to introduce either aqua or *tert*-butyl-isocyanide at the fourth coordination position. The comparative characterization of the obtained complexes was performed through several experimental techniques and DFT calculations. These studies showcase the versatility of the tripyrrindione platform for Pt(II) coordination. This tridentate, redox-active ligand allows for multicenter interactions between radicals of neutral complexes in solution as well as π-stacking and metallophilic interactions of cationic oxidized complexes in the solid state. Notably, the

monodentate ligand in the fourth coordination position (i.e., H_2O or tBuNC in this study) serves as a synthetic handle to modulate the properties of the complexes, including the redox potentials of predominantly tripyrrindione-based processes and the interactions between Pt(II) tripyrrindiones in solution and in the solid state.

Conflicts of interest

There are no conflicts to declare.

Acknowledgements

This work was supported by the National Science Foundation (award CHE-2203361 to E.T.), the Research Council of Norway (grant no. 324139 to A.G.), and the National Research Foundation of South Africa (grant nos. 129270 and 132504 to J.C.). The Bruker NEO-500 spectrometer in the UArizona Dept. of Chemistry and Biochemistry NMR Facility was purchased thanks to support from the National Science Foundation (MRI award CHE-1920234).

References

1 K. E. Preuss, *Polyhedron*, 2014, **79**, 1.
2 M. Kertesz, *Chem. Eur. J.*, 2019, **25**, 400.
3 T. Nishinaga and K. Komatsu, *Org. Biomol. Chem.*, 2005, **3**, 561.
4 R. S. Mulliken and W. B. Person, Wiley-Interscience, New York, 1969, pp. 259-259.
5 D. Yuan, W. Liu and X. Zhu, *Chem*, 2021, **7**, 333.
6 K. Cai, L. Zhang, R. D. Astumian and J. F. Stoddart, *Nat. Rev. Chem.*, 2021, **5**, 447.
7 J. Fajer, D. C. Borg, A. Forman, D. Dolphin and R. H. Felton, *J. Am. Chem. Soc.*, 1970, **92**, 3451.
8 J. H. Fuhrhop, P. Wasser, D. Riesner and D. Mauzerall, *J. Am. Chem. Soc.*, 1972, **94**, 7996.
9 H. Song, C. A. Reed and W. R. Scheidt, *J. Am. Chem. Soc.*, 1989, **111**, 6867.
10 G. Bottari, O. Trukhina, M. Ince and T. Torres, *Coord. Chem. Rev.*, 2012, **256**, 2453.
11 A. Takai, C. P. Gros, J.-M. Barbe, R. Guilard and S. Fukuzumi, *Chem. Eur. J.*, 2009, **15**, 3110.
12 A. I. Oliva, B. Ventura, F. Würthner, A. Camara-Campos, C. A. Hunter, P. Ballester and L. Flamigni, *Dalton Trans.*, 2009, 4023.
13 F. D'Souza, R. Chitta, S. Gadde, L. M. Rogers, P. A. Karr, M. E. Zandler, A. S. D. Sandanayaka, Y. Araki and O. Ito, *Chem. Eur. J.*, 2007, **13**, 916.
14 N. Fukui, W. Cha, D. Shimizu, J. Oh, K. Furukawa, H. Yorimitsu, D. Kim and A. Osuka, *Chem. Sci.*, 2017, **8**, 189.
15 A. Kumar, S. Sanfui, G. Sciortino, J.-D. Maréchal, E. Garribba and S. P. Rath, *Chem. Eur. J.*, 2020, **26**, 7869.
16 W. J. Kendrick, M. Jirásek, M. D. Peeks, G. M. Greetham, I. V. Sazanovich, P. M. Donaldson, M. Towrie, A. W. Parker and H. L. Anderson, *Chem. Sci.*, 2020, **11**, 2112.
17 S. Sarkar, P. Sarkar, D. Samanta, S. K. Pati and S. P. Rath, *ACS Catalysis*, 2022, **12**, 9589.
18 H. Tanaka, Y. Kobayashi, K. Furukawa, Y. Okayasu, S. Akine, N. Yasuda and H. Maeda, *J. Am. Chem. Soc.*, 2022, **144**, 21710.
19 Y. A. Pandit, M. Usman, A. Sarkar, S. J. Shah and S. P. Rath, *Dalton Trans.*, 2023, **52**, 877.
20 D. Shimizu and A. Osuka, *Chem. Sci.*, 2018, **9**, 1408.
21 A. L. Balch and F. L. Bowles, eds. K. M. Kadish, K. M. Smith and R. Guilard, World Scientific Publishing Co., Singapore, 2010, pp. 294-339.
22 E. Tomat, *J. Porphyrins Phthalocyanines*, 2019, **23**, 1265.
23 E. Tomat and C. J. Curtis, *Acc. Chem. Res.*, 2021, **54**, 4584.
24 C. J. Curtis, A. V. Astashkin, J. Conradie, A. Ghosh and E. Tomat, *Inorg. Chem.*, 2021, **60**, 12457.
25 R. Gautam, J. J. Loughrey, A. V. Astashkin, J. Shearer and E. Tomat, *Angew. Chem. Int. Ed.*, 2015, **54**, 14894.
26 S. Bahnmüller, J. Plotzitzka, D. Baabe, B. Cordes, D. Menzel, K. Schartz, P. Schweyen, R. Wicht and M. Bröring, *Eur. J. Inorg. Chem.*, 2016, **2016**, 4761.
27 R. Gautam, A. V. Astashkin, T. M. Chang, J. Shearer and E. Tomat, *Inorg. Chem.*, 2017, **56**, 6755.
28 R. Gautam, S. J. Petritis, A. V. Astashkin and E. Tomat, *Inorg. Chem.*, 2018, **57**, 15240.
29 A. Heil and C. M. Marian, *Phys. Chem. Chem. Phys.*, 2019, **21**, 19857.
30 M. Mauro, A. Aliprandi, D. Septiadi, N. S. Kehr and L. De Cola, *Chem. Soc. Rev.*, 2014, **43**, 4144.
31 V. W.-W. Yam and A. S.-Y. Law, *Coord. Chem. Rev.*, 2020, **414**, 213298.
32 M. Yamamura, H. Takizawa, Y. Gobo and T. Nabeshima, *Dalton Trans.*, 2016, **45**, 6834.
33 N. M. Shavaleev, E. S. Davies, H. Adams, J. Best and J. A. Weinstein, *Inorg. Chem.*, 2008, **47**, 1532.
34 G. Sanna, G. Minghetti, A. Zucca, M. I. Pilo, R. Seeber and F. Laschi, *Inorg. Chim. Acta*, 2000, **305**, 189.
35 P. S. Braterman, J. I. Song, F. M. Wimmer, S. Wimmer, W. Kaim, A. Klein and R. D. Peacock, *Inorg. Chem.*, 1992, **31**, 5084.
36 Y. Akdogan, C. Vogt, M. Bauer, H. Bertagnolli, L. Giurgiu and E. Roduner, *Phys. Chem. Chem. Phys.*, 2008, **10**, 2952.
37 K. E. Brancato-Buentello, S.-J. Kang and W. R. Scheidt, *J. Am. Chem. Soc.*, 1997, **119**, 2839.
38 J.-M. Lü, S. V. Rosokha and J. K. Kochi, *J. Am. Chem. Soc.*, 2003, **125**, 12161.
39 T. Vangberg, R. Lie and A. Ghosh, *J. Am. Chem. Soc.*, 2002, **124**, 8122.
40 H. S. La Pierre, J. Arnold, R. G. Bergman and F. D. Toste, *Inorg. Chem.*, 2012, **51**, 13334.
41 M. Yoshida and M. Kato, *Coord. Chem. Rev.*, 2018, **355**, 101.
42 V. W.-W. Yam, V. K.-M. Au and S. Y.-L. Leung, *Chem. Rev.*, 2015, **115**, 7589.
43 A. Aliprandi, D. Genovese, M. Mauro and L. De Cola, *Chem. Lett.*, 2015, **44**, 1152.
44 D. Blasco, F. Reboiro, D. Sundholm, M. E. Olmos, M. Monge and J. M. Lopez-de-Luzuriaga, *Dalton Trans.*, 2023, **52**, 2219.
45 Z.-h. Cui, H. Lischka, H. Z. Beneberu and M. Kertesz, *J. Am. Chem. Soc.*, 2014, **136**, 12958.
46 F. Glöcklhofer, *ChemRxiv*, 2023, DOI: 10.26434/chemrxiv.
47 J. Conradie, C. Foroutan-Nejad and A. Ghosh, *Sci. Rep.*, 2019, **9**, 4852.
48 E. van Lenthe, E. J. Baerends and J. G. Snijders, *J. Chem. Phys.*, 1993, **99**, 4597.
49 E. van Lenthe, E. J. Baerends and J. G. Snijders, *J. Chem. Phys.*, 1994, **101**, 9783.
50 N. C. Handy and A. Cohen, *Molecular Physics*, 2001, **99**, 403.
51 C. Lee, W. Yang and R. G. Parr, *Phys. Rev. B*, 1988, **37**, 785.
52 A. D. Becke, *J. Chem. Phys.*, 1993, **98**, 5648.

53 P. J. Stephens, F. J. Devlin, C. F. Chabalowski and M. J. Frisch, *J. Phys. Chem.*, 1994, **98**, 11623.
54 S. Grimme, J. Antony, S. Ehrlich and H. Krieg, *J. Chem. Phys.*, 2010, **132**, 154104.
55 G. te Velde, F. M. Bickelhaupt, E. J. Baerends, C. Fonseca Guerra, S. J. A. van Gisbergen, J. G. Snijders and T. Ziegler, *J. Comput. Chem.*, 2001, **22**, 931.